The Astrophysical Journal, 934:148 (17pp), 2022 August 1 https://doi.org/10.3847/1538-4357/ac78d9

Testing White Dwarf Age Estimates Using Wide Double White Dwarf Binaries from Gaia EDR3

Tyler M. Heintz[1], J. J. Hermes[1], Kareem El-Badry[2,3], Charlie Walsh[1], Jennifer L. van Saders[4], C. E. Fields[5,6,7,9], and Detlev Koester[8]

[1G] Department of Astronomy & Institute for Astrophysical Research, Boston University, 725 Commonwealth Avenue, Boston, MA 02215, USA; tmheintz@bu.edu
[2] Center for Astrophysics |Harvard & Smithsonian, 60 Garden Street, Cambridge, MA 02138, USA
[3] Harvard Society of Fellows, 78 Mount Auburn Street, Cambridge, MA 02138, USA
[4] Institute for Astronomy, University of Hawai'i, 2680 Woodlawn Drive, Honolulu, HI 96822, USA
[5] Center for Theoretical Astrophysics, Los Alamos National Laboratory, Los Alamos, NM 87545, USA
[6] Computer, Computational, and Statistical Sciences Division, Los Alamos National Laboratory, Los Alamos, NM 87545, USA
[7] X Computational Physics Division, Los Alamos National Laboratory, Los Alamos, NM 87545, USA
[8] Institut für Theoretische Physik und Astrophysik, University of Kiel, D-24098 Kiel, Germany
Received 2022 March 15; revised 2022 May 25; accepted 2022 June 8; published 2022 August 2

Abstract

White dwarf (WD) stars evolve simply and predictably, making them reliable age indicators. However, self-consistent validation of the methods for determining WD total ages has yet to be widely performed. This work uses 1565 wide (>100 au) WD+WD binaries and 24 new triples containing at least two WDs to test the accuracy and validity of WD total age determinations. For these 1589 wide double WD binaries and triples, we derive the total age of each WD using photometric data from all-sky surveys, in conjunction with Gaia parallaxes and current hydrogen atmosphere WD models. Ignoring the initial-to-final mass relation and considering only WD cooling ages, we find that roughly 21%–36% of the more massive WDs in a system have a shorter cooling age. Since more massive WDs should be born as more massive main-sequence stars, we interpret this unphysical disagreement as evidence of prior mergers or the presence of an unresolved companion, suggesting that roughly 21%–36% of wide WD+WD binaries were once triples. Among the 423 wide WD+WD pairs that pass high-fidelity cuts, we find that 25% total age uncertainties are generally appropriate for WDs with masses $>0.63\,M_{\odot}$ and temperatures <12,000 K and provide suggested inflation factors for age uncertainties for higher-mass WDs. Overall, WDs return reliable stellar ages, but we detail cases where the total ages are least reliable, especially for WDs $<0.63\,M_{\odot}$.

Unified Astronomy Thesaurus concepts: White dwarf stars (1799); Wide binary stars (1801); Stellar ages (1581)

Supporting material: machine-readable table

1. Introduction

White dwarf (WD) stars are the end stage of all stars with initial masses of less than roughly $8-10\,M_{\odot}$ (Doherty et al. 2015) and have been used for decades as stellar chronometers (see review by Fontaine et al. 2001). Since WDs no longer undergo core fusion, their evolution is generally a cooling problem. The development of robust cooling models (e.g., Bergeron et al. 1995) enables WDs to act as precise and accurate age indicators. However, to determine the total age of a WD, the time from the zero-age main sequence (ZAMS) to the current state of the WD is required. The progenitor lifetimes from ZAMS to the WD phase are determined through the use of a semiempirical initial–final mass relation (IFMR; Catalán et al. 2008; Kalirai et al. 2008; Salaris et al. 2009; Cummings et al. 2018) in conjunction with stellar evolution model grids, such as MESA (Dotter 2016) and PARSEC (Bressan et al. 2012).

The total ages of WDs can be used to date a variety of astronomical objects, including wide binary companions, such as M dwarfs (e.g., Fouesneau et al. 2019; Kiman et al. 2021; Qiu et al. 2021), brown dwarfs (Zhang et al. 2020), and a growing number of planet-host stars (Martin et al. 2021). The WDs can also age-date larger populations, such as stars in the disk (e.g., Winget et al. 1987) or even the halo of our Galaxy (Kilic et al. 2019; Torres et al. 2021). The ages of WDs can also be used to study the star formation history of the Milky Way (e.g., Tremblay et al. 2014). An understanding of the limitations and reliability of WD total ages is crucial to the inferences derived from these studies.

The total age derived for a WD is strongly dependent on the IFMR used, especially for the lowest-mass WDs ($M < 0.7\,M_{\odot}$). However, the low-mass region of the IFMR is poorly sampled because nearby clusters containing at least one WD are not old enough. Attempts have been made to alleviate this problem by using wide binary companions to WDs (Zhao et al. 2012; Barrientos & Chanamé 2021) and the distribution of WDs in the color–magnitude diagram (CMD; El-Badry et al. 2018), but this still results in a large range of predicted progenitor masses across different IFMRs. Further, the IFMR may show evidence of a kink where the mass-loss relationship is no longer monotonic (Marigo et al. 2020). The IFMR is likely also sensitive to the metallicity and initial rotation of the progenitor star (Cummings et al. 2019). These parameters are not easy to determine; thus, assumptions for their values must be made.

Widely separated double WD binaries (WD+WD binaries) are ideal systems for checking the viability of our existing methods for determining WD total ages. It is safe to assume the

[9] Feynman Fellow.

two WDs bound to each binary system formed from the same collapsing molecular cloud at nearly the same time with the same chemical composition (White & Ghez 2001; Kraus & Hillenbrand 2009). Wide WD+WD binaries that are sufficiently separated (>100 au) have not experienced any significant mass transfer events or other interactions between the two stars during their lifetimes. At intermediate separations (1–100 au), where tidal forces, mass transfer, and accretion are not a significant source of interaction, it has been shown that the interaction between a companion and the circumstellar disk can affect the angular momentum evolution of the star (Morgan et al. 2012). In the absence of any interactions between the two stars, any methods for determining the total age of a WD should independently return the same total age for both components of the binary.

Since the launch of the Gaia spacecraft (Gaia Collaboration et al. 2016, 2018a, 2021), the sample of wide WD+WD binary systems has increased by an order of magnitude (Andrews et al. 2015; El-Badry & Rix 2018; Tian et al. 2020; El-Badry et al. 2021). This increase in systems presents the opportunity for a large statistical study into the accuracy of the models and methods used to determine the total ages of WDs, which is the focus of this work. In Section 2, we present the sample selection of resolved WD+WD binary systems, including 23 new WD+WD+MS systems and one bound WD+WD+WD system. Section 3 discusses the techniques used to determine their ages. In Section 4, we discuss comparisons of the total ages in each binary. We end with a summary of the findings and results in Section 5.

2. Sample Selection

Obtaining a large sample of wide double WD pairs is crucial for this work. The improved parallaxes and proper motions for more than 1 billion sources all-sky with the release of Gaia EDR3 (Gaia Collaboration et al. 2021) significantly increased the potential yield of searches for wide common proper-motion pairs. With this larger sample, we can delve into the systematic errors present in WD total age determinations.

2.1. Binary Sample

For this work, the base of our sample is composed of the 1565 wide WD+WD binaries from El-Badry et al. (2021). Candidate pairs in this work were selected to have projected separations of less than a parsec, parallaxes that are consistent within 3σ, and proper motions consistent within 2σ of a bound orbit. This sample is restricted to objects with fractional parallax uncertainties less than 20% for both components, with most systems within 300 pc. The sample covers a wide range of magnitudes, spanning 13 mag $< G <$ 21 mag, with roughly 68% of the 3130 individual WDs in the sample fainter than $G > 19$ mag.

El-Badry et al. (2021) calculated a chance alignment factor (`R_chance_align`) for each candidate binary pair through the use of a shifted Gaia catalog. Conducting a search for binaries in the shifted catalog only produces chance alignments and thus can be used as a way to determine the likelihood that a binary pair is a chance alignment (see their Section 3). This parameter can be used to filter out low-fidelity wide binaries.

2.2. Triple Sample

To further increase the sample of wide double WDs, we conduct a search for wide, resolved triple star systems containing at least two WDs. In El-Badry et al. (2021), all triple systems are intentionally removed from the sample by the neighboring pairs cut (see their Section 2.1). In this work, we take the sample of binary pairs from El-Badry et al. (2021) before the cleaning of the sample and remove the neighboring pairs cut but retain the cut on neighboring sources of $N < 30$, where a neighboring source is defined, following El-Badry et al. (2021), as a source with (i) a projected on-sky separation of less than 5 pc, (ii) a proper-motion difference of less than 5 km s^{-1} with a 2σ tolerance, and (iii) parallaxes consistent within 2σ.

Next, we make a list of systems of various sizes by combining all binaries with at least one common source between them. We iterate this process until each system is independent of each other.

To clean this new sample of possible wide systems, we use the classifier for spurious astrometric solutions provided in Rybizki et al. (2022). We require each component of the triple to have a `fidelity_v1` parameter greater than 0.5. This ensures that each source has a reliable astrometric solution. We are only concerned with finding systems with three components in this extended list and throw out any systems with a size not equal to 3. (Repeating this exercise for $N = 4, 5, \ldots$, we do not find any systems with a size greater than 3 in this extended list of wide systems with at least two WDs.)

With these cuts, we identify 23 new WD+WD+MS triples and one WD+WD+WD triple. This list includes the first resolved triple WD system found by Perpinyá-Vallés et al. (2019). All WD+WD+MS and WD+WD+WD triple systems are detailed in Table A2. All but three of the triples in our sample are hierarchical, where we have defined a hierarchical triple as one in which the largest separation is greater than five times the smallest separation. An excess of hierarchical triples is expected, since the hierarchy improves the dynamical stability in the system (Hut & Bahcall 1983).

The total ages in the nonhierarchical systems (WDWDMS EDR3 3681220906103896192, WDWDMS EDR3 6756233901661753472, WDWDMS EDR3 9290018083-77561216) can provide interesting constraints on the timescales of dissipation of such systems. In both WDWDMS EDR3 3681220906103896192 and WDWDMS EDR3 6756233901661753472, one of the WDs does not have a total age estimate, since it has a mass of 0.2 and 0.35 $M_\odot$, respectively, but the total ages of the other WDs in these triples are 92^{+3}_{-5} Myr and $2.9^{+0.4}_{-0.2}$ Gyr, respectively. The weighted mean total age of the WDs in WDWDMS EDR3 929001808377561216 is $3.3^{+3.1}_{-1.3}$ Gyr. Further information is found in Table A2.

Although two of these nonheirarchical wide triples seem too old (>2.5 Gyr) to still be bound, it has recently been shown that the unstable phase of these triples, on average, lasts 10^3–10^4 crossing times and can even last as long as 10^6–10^7 (Toonen et al. 2021). Assuming the crossing time is of similar magnitude to the outermost orbital period, the two older systems would have a crossing time of $\sim 10^4$ yr, indicating that the older systems have experienced $\sim 10^5$ crossing times. Of the 21 systems that are hierarchical, 19 systems have an inner pair of two WDs, although this is likely an observational bias caused by the high luminosity ratio of a main-sequence (MS) star to a WD.

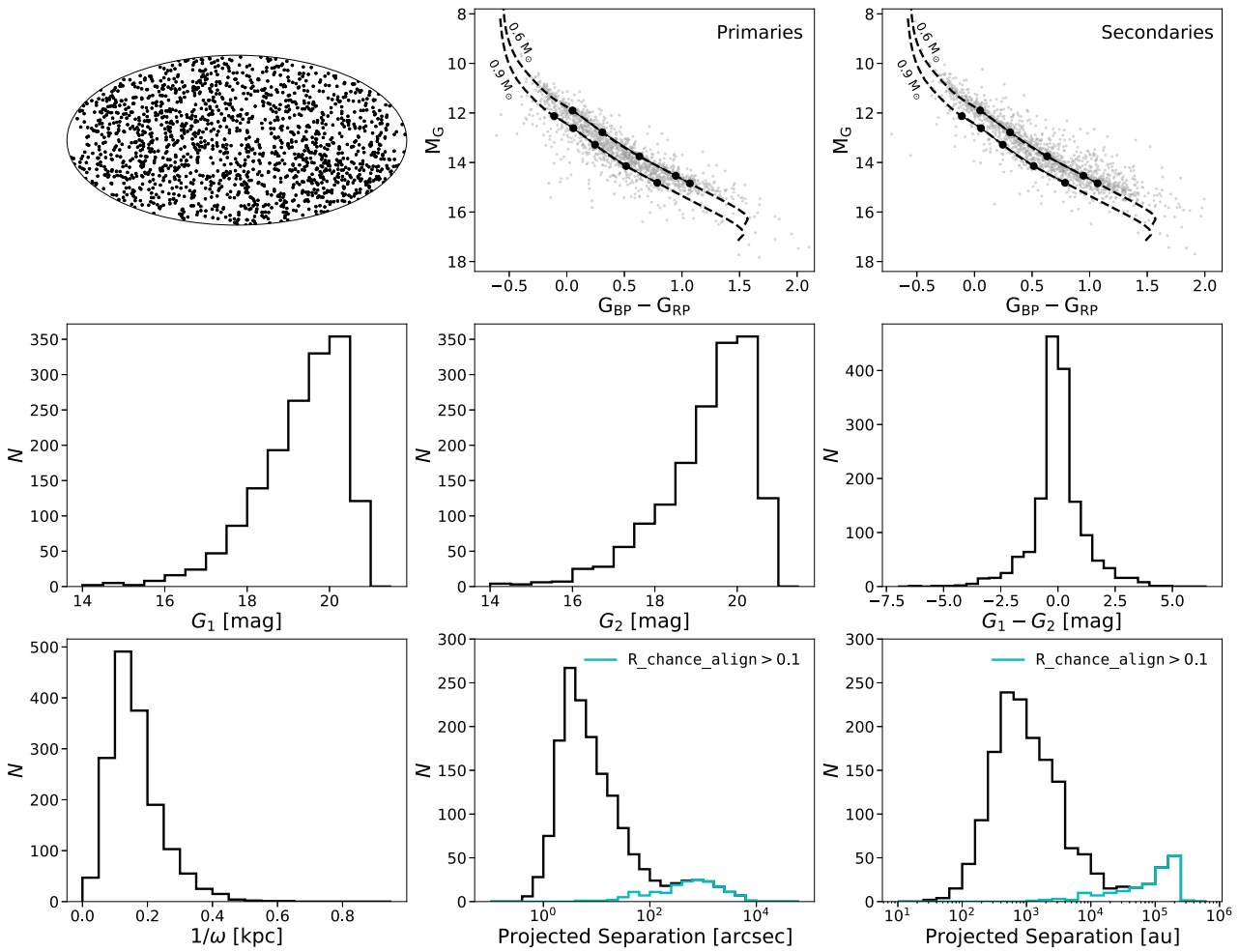

Figure 1. Basic properties of the full sample of 3179 WDs in wide WD+WD binaries from El-Badry et al. (2021) used in this work, including 23 of our newly discovered wide WD+WD+MS triples and one WD+WD+WD triple: distribution in galactic coordinates, CMDs for the primaries and secondaries, apparent magnitude distributions, magnitude differences, distances, and projected angular and physical separations. The primaries are defined to be the more massive WD component. A large range of the WD cooling tracks is covered by the sample, which allows us to test the total ages of WDs across a representative sample of WD masses and effective temperatures. Cooling tracks for a 0.6 and 0.9 $M_{\odot}$ WD model from Bédard et al. (2020) are shown for reference on the CMDs, as well as dots representing WD cooling ages of 0.5, 1, 2, 4, and 6 Gyr for each. The separation distribution of pairs with `R_chance_align` > 0.1 is shown in cyan for reference in the bottom middle and right panels. The upturn in the distribution at high separations is caused by these possible chance alignments.

Our search is sensitive to wide triple WD systems, but we do not find any new wide WD+WD+WD systems. We do find a possible candidate for a new WD+WD+WD system (Gaia EDR3 source IDs 261249666477351552, 261249670772776832, and 261249636413169920), but one component has a `fidelity_v1` parameter from Rybizki et al. (2022) of 0.01. Still, all three WDs have significant parallaxes and proper motions that are in better than 2σ agreement. With all components $G > 20$ mag, this potential new WD+WD+WD is significantly fainter than the first published triple WD system. This limits the parallaxes of each WD to 10%–15% uncertainties. The system lies somewhere between 100 and 130 pc, with the weighted mean distance being 118 ± 8 pc. This possible WD triple has a similar hierarchy as the first such identified system in Perpinyá-Vallés et al. (2019); the system has an inner pair separated by ≈170 au and an outer component separated by ≈6500 au. (The first triple WD system has an inner separation of ≈300 au and outer separation of ≈6400 au.) Follow-up analysis is needed to confirm the true nature of this possible WD+WD+WD system.

2.3. Full Sample

Various parameter distributions of the full sample, including a CMD of all wide double WDs, is shown in Figure 1. Our full sample of wide WD+WD pairs spans a large range of the WD cooling sequence, covering many masses and effective temperatures. The sample also spans many different evolutionary stages. In fact, we expect roughly 430 WDs (13%) to be mostly crystallized, based on the 80% crystallization boundary from Tremblay et al. (2019). However, many of our targets are quite faint; the majority of sources are fainter than $G >$ 19.5 mag (see Figure 1). The separation distribution shows an excess of high-separation pairs. These pairs are likely chance alignments and can be removed with a cut on `R_chance_align` from El-Badry et al. (2021), as discussed in Section 4.

In preparation for the eventual total age determination, we gather additional photometric data on each WD in order to sample a larger range of wavelengths than just the three broad photometric bands in Gaia EDR3. We use the crossmatches provided by the Gaia team for EDR3 (Marrese et al. 2021) to

get photometric data from the Sloan Digital Sky Survey (SDSS), the Panoramic Survey Telescope and Rapid Response System (PanSTARRS), the SkyMapper Southern Survey, and the Two Micron All Sky Survey (2MASS). We find that 32%, 70%, 23%, and 4% of the WDs in our sample have photometry in SDSS, PanSTARRS, Skymapper, and 2MASS, respectively.

3. Total Age Determination

The total ages of WDs have two necessary components that need to be determined: the time the star has spent as a WD (its cooling age) and its progenitor MS and giant branch lifetimes. To calculate the cooling age of a WD, the atmospheric parameters of the WD must be determined, which can be derived using either spectroscopic or photometric data in conjunction with model atmospheres. Fundamentally, the WD surface gravity and temperature must be determined.

Spectroscopic observations are available in the literature for roughly 300 of the WDs in our sample, so we lack spectroscopy for the vast majority of our 3179 objects. Therefore, we resort to conducting spectral energy distribution (SED) fitting of the average fluxes in various photometric bands from all-sky surveys. In practice, SED fitting is sensitive to the radius and temperature of a WD. This radius can be converted into a surface gravity through the use of the mass–radius relationship for WDs (Bédard et al. 2020).

Once a surface gravity and temperature are determined, an estimate of the mass of the WD can be calculated using the same mass–radius relationship. This estimate of the mass, with the use of an IFMR and stellar evolutionary grids, can be used to generate an estimate of the lifetime of the ZAMS progenitor. We discuss this process in more detail below.

3.1. WD Atmospheric Parameters

To determine the masses and effective temperatures of the WDs in our sample, we use available photometry from Gaia EDR3 and the all-sky surveys discussed in Section 2.3, in conjunction with a fitting technique similar to the photometric technique described in Bergeron et al. (2019).

Reddening effects from interstellar gas and dust can be important for the WDs in our sample (the majority are at a distance beyond 150 pc). Thus, the observed magnitudes in each band are dereddened following the process outlined in Gentile Fusillo et al. (2019), which we summarize here. We use reddening maps from Schlafly & Finkbeiner (2011) to determine the extinction coefficient in the Johnson V band, A_V. Then, the A_V values are converted to extinction coefficients in the other bands using the appropriate R values. We assume the material is concentrated along the galactic plane and has a scale height of 200 pc. When parameterized this way, the dereddened magnitude in a given band X is determined by

$$M_{\rm x} = M_{\rm x,obs} - A_{\rm x}\left(1 - \exp\left(-\frac{\sin(|b|)}{200\omega}\right)\right), \quad (1)$$

where $M_{\rm x,obs}$ is the observed magnitude, $A_{\rm x}$ is the extinction coefficient, b is the galactic latitude, and ω is the parallax in arcseconds. A more sophisticated reddening determination can be used similar to what is done in Gentile Fusillo et al. (2021), but in comparisons with atmospheric parameters derived in their work, we find no systematic shifts, and the parameters are in good agreement (as demonstrated below).

The observed, dereddened magnitudes are converted to average fluxes using the appropriate zero-points for each bandpass. We apply the G-band magnitude correction for all sources with a six-parameter astrometric solution provided in Gaia Collaboration et al. (2021). To account for the offset of SDSS magnitudes from the AB magnitude standard, we apply an offset of -0.04 and 0.02 mag in the u and z band, respectively (Eisenstein et al. 2006). For each survey, we remove photometry that has been flagged for various issues. For SDSS, we remove photometry that has been flagged with `EDGE`, `PEAKCENTER`, `SATUR`, and `NOTCHECKED`. We remove photometry from PanSTARRS that uses rank detections less than 1. For SkyMapper, we only use photometry that has no raised flags. We also enforce a minimum uncertainty in each bandpass of 0.03 mag to account for systematic errors in the conversion of magnitudes to average fluxes. This also gives equal weight to each bandpass, and one point with a small error will not dominate the behavior of the fits.

We generate synthetic averages fluxes in a given bandpass using synthetic hydrogen atmosphere WD (spectral type DA) spectra from Koester (2010), convolved with the appropriate filter transmission profiles. The observed and synthetic fluxes are adjusted to a distance of 10 pc using the weighted mean of the parallaxes of the two components of the binary or the weighted mean of all three components for our triples. To adjust the synthetic fluxes to 10 pc, the radius of the WD must be calculated from a mass–radius relation. We use the WD evolutionary models from Bédard et al. (2020) to convert the temperature and surface gravity of a given model to a radius. The photometric uncertainties are then added in quadrature with the uncertainty on this weighted mean parallax. The use of the weighted parallax in these systems allows for more precise determinations of the atmospheric parameters due to its higher precision. For the sample of triples, the precision of the parallax is six times better, on average, because the MS companions are much brighter. This leads to the WDs in these triples having smaller mass uncertainties than what is expected given their brightness (an average improvement of 40% for the brighter WD component and 15% for the fainter WD component).

Due to the lack of spectral information for the majority of our objects, we assume that all of our WDs are DAs. Although fitting a non-DA WD with a DA model can introduce systematic mass errors on the order of 10%–15% (Giammichele et al. 2012), we are forced to choose a model. A DA model is the simplest assumption, considering >65% of WDs in magnitude-limited samples within Gaia are DAs (Kleinman et al. 2013).

We use the python package emcee (Foreman-Mackey et al. 2013), which uses an affine invariant Markov Chain Monte Carlo (MCMC; Goodman & Weare 2010), to get the posterior range on the temperature and surface gravity for each WD in the sample. We use the 50th percentile of these posteriors as an estimate of the best fit. We use flat priors on both effective temperature and surface gravities with bounds defined from the limits of the models (3000–40,000 K and log$g$ of 6.0–9.5 dex) and assume Gaussian errors. Using the WD evolutionary models from Bédard et al. (2020), which assume thick H layers, we convert the surface gravities and temperatures to masses and cooling ages. The lower and upper errors on these parameters are taken as the 16th and 84th percentiles, respectively. To account for any unknown systematics, we set a lower limit on the uncertainty of the atmospheric

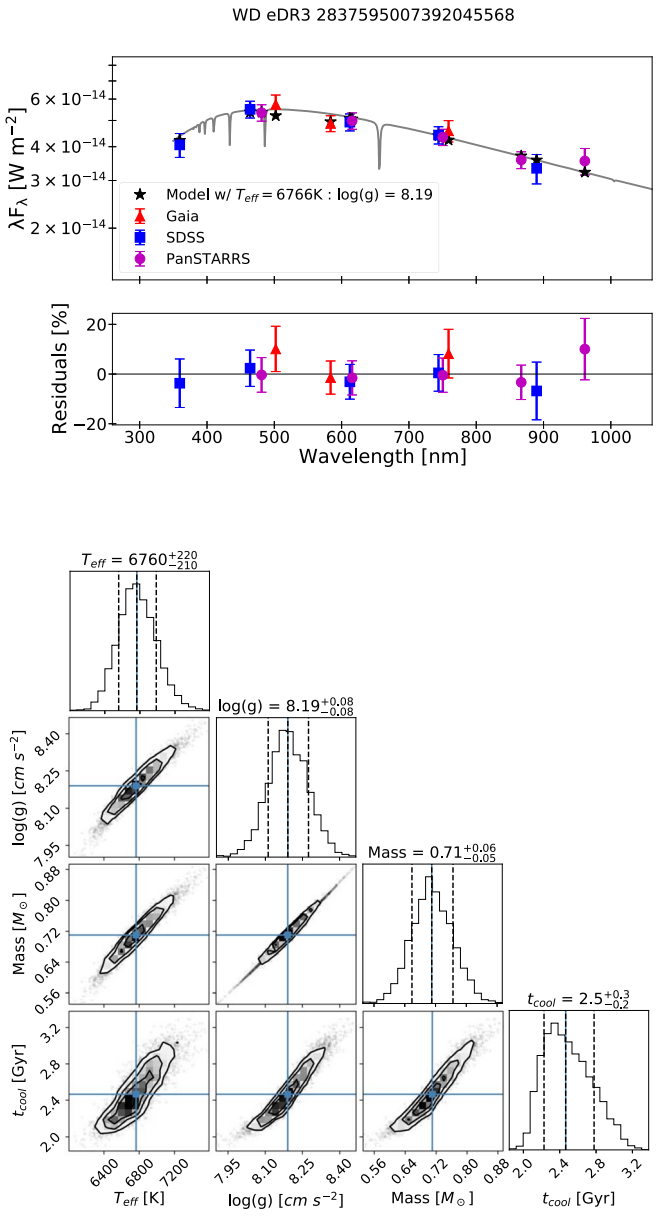

Figure 2. Example fit to get the atmospheric parameters of our WDs. The top two panels show the SED, including all observed photometry and a representative atmospheric model, as well as the residual from the fit. The posterior distributions from the MCMC fitting code used in this work are shown in the bottom part of the figure.

parameters derived from the fits of 0.038 dex for surface gravity and 1.2% in temperature (Liebert et al. 2005). An example of a fit can be seen in Figure 2.

As a check on our methods, we compare the atmospheric parameters we derive to the parameters from the 100 pc WD sample of Kilic et al. (2020) and the full Gaia EDR3 WD catalog from Gentile Fusillo et al. (2021), which were also determined from the photometric technique we employ. The comparison to the 100 pc WD sample from Kilic et al. (2020) reveals no significant systematic differences between the two works. The atmospheric parameters, on average, agree within 0.9σ (100 K) and 0.6σ (0.03 dex) for effective temperature and surface gravity, respectively. We observe some small dispersion at higher temperatures, which we expect, since our work incorporates interstellar reddening, whereas Kilic et al. (2020) did not. Comparing to the Gaia EDR3 WD catalog, we find that the atmospheric parameters, on average, agree within 0.4σ (300 K) and 0.35σ (0.1 dex) for effective temperature and surface gravity, respectively. The quoted uncertainties we find are significantly smaller than the ones in Gentile Fusillo et al. (2021) due to the use of more photometric points in the SED and the weighted parallax. Although we have smaller uncertainties and use different methods to determine the amount of interstellar reddening, we do not find any systematic shifts in the derived WD atmospheric parameters.

We also search for the spectral types of our objects that have been published in the literature, finding 305 objects with previously reported spectra. The sources for these spectral types can be found in the catalog of WD pairs described in Table A1.

We supplement these previously published spectral types with 57 spectra taken on the DeVeny Spectrograph mounted on the 4.3 m Lowell Discovery Telescope (LDT; Bida et al. 2014) in Happy Jack, Arizona. Using a 300 line mm^{-1} grating, we obtain a roughly 4.5 Å resolution and rotate the position angle of the slit to capture both WDs simultaneously in our observations. We extract the spectra using a quick-look pipeline written using the ccdproc and specutils packages from the AstroPy package (Astropy Collaboration et al. 2018) and wavelength-calibrate the spectra with a HgArNe lamp. We do not attempt to fit these spectra and only conduct a visual inspection for the presence of hydrogen absorption features; we include their spectral type in the sp_type column described in Table A1. Future work will further analyze the atmospheric parameters derived from this spectroscopy.

Comparing the derived atmospheric parameters of the previously identified DAs with the parameters derived in this work, we find that the effective temperatures agree well but that the determination of the surface gravities from spectroscopic observations vary from our own values derived from photometric information. We find that the atmospheric parameters of our work and the spectroscopic parameters, on average, agree within 0.9σ (300 K) and 1.3σ (0.1 dex) for effective temperature and surface gravity, respectively. We also find that the spectroscopic fits find higher surface gravities for the WDs, on average, and thus hotter temperatures as well. Although the absolute differences are similar to the other comparisons, the quoted uncertainties from the spectroscopic parameters are smaller and result in a stronger disagreement in surface gravity (1.3σ compared to 0.9σ and 0.35σ).

3.2. Initial Masses and Progenitor Lifetimes

To get the total ages of the WDs in our sample, we need an estimate of the lifetime of the ZAMS progenitor. The first step toward this is to determine an initial MS mass for each of the WDs in our sample. To get these masses, an IFMR is needed. In this work, we use the theoretical IFMR from Fields et al. (2016), which was generated by running a suite of solar metallicity stellar evolution models from the Modules for Experiments in Stellar Astrophysics (MESA; Paxton et al. 2011, 2013, 2015) starting at the pre-MS phase through the thermally pulsing asymptotic giant branch to the final WD phase. This allows us to remain self-consistent within both our IFMR and our determination of ZAMS progenitor lifetimes using the same open-source stellar evolution code and to use a more theoretically motivated shape for the IFMR.

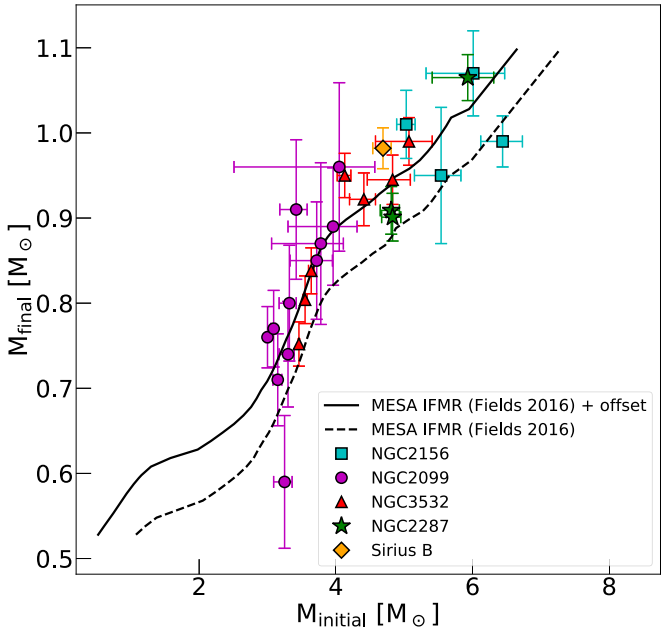

Figure 3. The IFMR used in this work to connect a WD mass to a single ZAMS progenitor mass. The dashed line shows the theoretical IFMR from MESA calculated by Fields et al. (2016). The observational data points are WDs in solar metallicity clusters along with Sirius B from Catalán et al. (2008) and Cummings et al. (2015, 2016). The solid line shows our adopted IFMR, which includes a constant y-axis offset of $+0.0636\,M_\odot$ found as a best fit to the cluster observations (the values for which are in Table B1).

The theoretical IFMR (shown as the dashed line in Figure 3) lies below what is observed for WDs in near-solar metallicity clusters, an effect that is still not fully understood but might involve uncertainties in the amount of convective overshoot that is used in the models (Fields et al. 2016) or in nuclear reaction rates that can affect the core mass (e.g., deBoer et al. 2017). To account for this systematic effect, we fit a positive offset to the IFMR using the same WDs in solar metallicity clusters. We find that the best-fitting offset to apply to the final WD mass is $+0.0636\,M_\odot$. The points of this shifted IFMR can be found in Table B1.

Using this modified IFMR (solid line in Figure 3), we generate progenitor MS masses for all of the WDs in our sample. We convert these MS masses into progenitor lifetimes by interpolating the solar metallicity zero-rotation MESA evolutionary tracks of Dotter (2016) and Choi et al. (2016) and summing the MS and giant branch lifetimes.

The uncertainties on the progenitor MS masses and lifetimes are determined by taking the 1σ uncertainties on the WD mass determined from the model atmosphere fitting described in Section 3.1, which determine an upper and a lower limit on the MS mass. Then the uncertainty on the progenitor lifetime is quoted as the difference between these 1σ bounds and the determined value. Total ages are then determined through the sum of the cooling age and the progenitor lifetime, and the uncertainties on total age are calculated by adding the uncertainties on cooling age and progenitor lifetime in quadrature. A table of all double WD pairs with atmospheric parameters and total ages can be accessed as supplemental data; a description of the table columns and data can be seen in Table A1.

As a check, we compare the progenitor lifetimes from our MESA IFMR to ones derived from the three-piece, cluster-calibrated IFMR from Cummings et al. (2018). We find that the progenitor lifetimes from both IFMRs are within 25% of each other, on average. The difference between the total ages is, on average, 10% when comparing the two IFMRs. Overall, we find that the use of the IFMR from Cummings et al. (2018) does not significantly change the conclusions discussed in subsequent sections.

3.3. Precision of Total Ages

The WD mass is the dominant factor for determining the total age of the WDs in our sample, and subsequently, the uncertainties in the WD mass strongly influence the degree of precision on the total ages.

This is especially true for the lower-mass WDs. For a typical $0.6\,M_\odot$ WD (Kepler et al. 2007; Tremblay et al. 2016), the initial progenitor MS mass is around $1.2\,M_\odot$, which corresponds to a progenitor lifetime of $\approx$6 Gyr. A 5% decrease in the WD mass results in a ZAMS progenitor mass of $0.88\,M_\odot$ and a progenitor lifetime of around 17 Gyr. Thus, for WDs near this mass range, it is extremely difficult to constrain the total age without very precise WD mass estimates. This problem is compounded by the fact that the lower-mass region of the IFMR is the least constrained. Depending on the IFMR used, initial mass values for a $0.6\,M_\odot$ WD can range between 1.2 and $2\,M_\odot$, which corresponds to progenitor lifetimes between 1.4 and 6 Gyr. This problem is also exaggerated when considering that for these low-mass WDs, the progenitor lifetimes are a major fraction of the total age.

We stress that low-mass WDs are still useful in providing a lower limit on total ages. A $0.6\,M_\odot$ WD with a 5% error on its mass can provide a 1σ lower limit of 1.4 Gyr on the progenitor lifetime, modulo uncertainties on the IFMR used. This, in conjunction with a precise cooling age, can still provide useful information on these WDs and their companions.

Fortunately, the opposite is true for the higher-mass WDs. Higher-mass WDs ($>0.8\,M_\odot$) come from massive progenitors, which have short ZAMS progenitor lifetimes. Thus, even larger mass uncertainties for high-mass WDs do not result in large errors on the progenitor lifetime (see Figure 4). Put another way, high-mass WDs can have large relative uncertainties in their progenitor lifetimes but still have relatively precise total ages. Additionally, the IFMRs of these high-mass WDs are better empirically constrained from cluster WDs.

4. Coeval Analysis

Before engaging in any analysis of the total ages, we remove systems where we know that our methods described in the previous section return unreliable total ages. We apply cuts on the sample to remove all systems with on-sky separation of $<2''$, as well as systems with `R_chance_align` < 0.1. We also remove systems with at least one component with $T_{\rm eff} < 3200$ K, as well as those with an inferred total age >14 Gyr.

The cut to on-sky separation removes systems with significant blending of the photometry, which confuses the SED fits (154 of the WD pairs have on-sky separations of $<2''$). We adopt the cut on the `R_chance_align` parameter provided in El-Badry et al. (2021); cutting at 0.1 ensures that the remaining systems have a high probability of being bound ($>$90%). Although we cut on a $<$10% chance alignment probability, we emphasize that the expected contamination

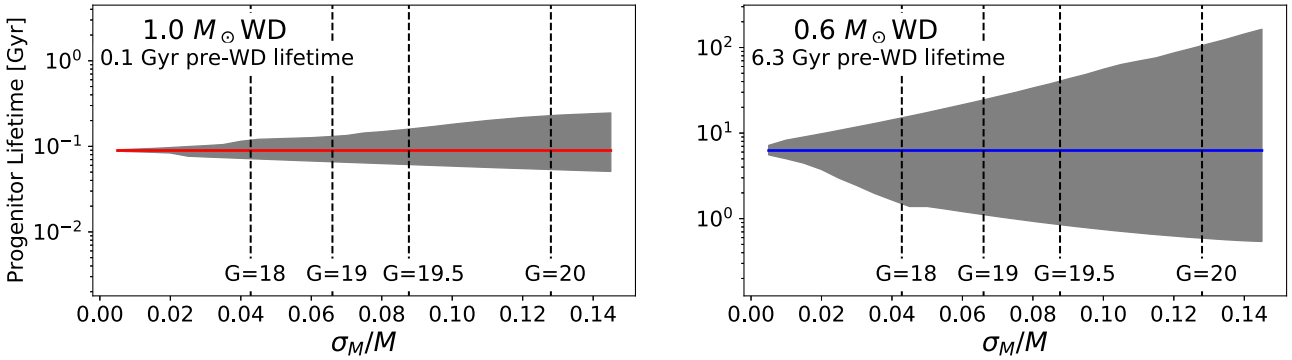

Figure 4. Visualization of how the precision on the ZAMS progenitor lifetime changes as a function of the WD mass uncertainty for a 1.0 (left) and 0.6 (right) $M_\odot$ WD. The gray shaded regions represent the 1σ uncertainties on the progenitor lifetimes. The axes are scaled to show the relative sizes of the uncertainties. The ZAMS progenitor lifetimes are given in the top left corner of each plot. The dashed vertical lines show the average relative uncertainty on the WD mass at a given *G*-band magnitude. The uncertainty on the WD mass is also affected by the precision of the parallax; thus, for a given *G*-band magnitude, there is some dispersion where more precise parallaxes give better mass constraints.

fraction from chance alignments is much less than 10%, because most of the pairs in the sample have chance alignment probabilities that are much lower than 10%. From the actual chance alignment probabilities of the pairs in our sample, we estimate that there are 4 ± 2 chance alignments in the sample, corresponding to a contamination fraction of about 0.3%. The wide WD+WD sample contains 1390 high-fidelity pairs with `R_chance_align` < 0.1 (see Figure 1).

The cut on effective temperature is employed because our model grid stops at 3000 K. Since our fitting routine does not attempt to extrapolate, objects with reported temperatures near the cutoff will have underestimated uncertainties, and their temperatures will be artificially hotter than their true temperatures. We also ignore all systems with a total age greater than that of the universe. Many of these systems come from overluminous sources in the Gaia CMD (see Figure 1). These sources will have low WD masses that, if they are actually so low mass, could not have formed from single-star evolution. At lower temperatures, the observed WD sample does not follow the cooling model trends, which may result in these lower unreliable masses (see Figure 1). There are a total of 670 WDs with inferred total ages >14 Gyr, which results in 548 pairs being removed.

After these cuts, the high-fidelity sample used for analysis contains 1272 WDs in 636 wide double WD pairs. The mean magnitude of this surviving sample is $G = 19.3$ mag.

4.1. Age Comparison

The first test of the total ages made is to check the absolute age difference in each pair. Since we assume that the stars in each wide pair in our sample are coeval, we expect them to return identical total ages. This absolute age difference is plotted in Figure 5. The total age difference between each component is typically close to zero until one of the component masses is below a value of $\sim 0.63\ M_\odot$. These systems do not provide very precise ages, and it is evident that the systematic uncertainty in these systems is too large to provide statistically significant comparisons.

This leads us to remove any systems that have a WD with a mass less than $0.63\ M_\odot$ from any further analysis. These systems can still be useful to provide lower limits on the total age, as discussed in Section 3.3, but we are not able to assess their reliability due to the large systematics in conjunction with their large uncertainties. After removing these systems, the number of wide WD+WD pairs is reduced to 423, with a total of 846 WDs.

The second test of the accuracy of the total ages is to compare the ages of the WDs in each binary in relation to the uncertainties on those total ages. To do this, we explore distributions of age agreement, which we define as

$$\sigma_{1-2} = \frac{\Delta\tau}{\sigma_{\Delta\tau}} = \frac{\tau_1 - \tau_2}{\sqrt{\sigma_{\tau_1}^2 + \sigma_{\tau_2}^2}}, \quad (2)$$

where τ_1 and $\sigma_{\tau 1}$ are the total age and uncertainty on the total age of the primary (the most massive component of each binary), and τ_2 and $\sigma_{\tau 2}$ are the total age and uncertainty on the total age of the less massive component. Systems with an age agreement (σ_{1-2}) equal to 5 have individual component ages that disagree at a 5σ level.

We show in Figure 6 the distribution of the σ_{1-2} disagreement for the 423 high-fidelity pairs where both WDs have $M > 0.63\ M_\odot$. The distribution exhibits a long tail out to large absolute values and has a notable bias toward negative values. Fewer than half (47%) of the systems have total age agreement within 1σ. The slight tendency toward negative σ_{1-2} disagreement values shows that the more massive component of each pair has a younger total age, on average, compared to its companion. Possible causes of this asymmetry are further explored in Section 4.2. The long tail of the distribution reveals that there is a population of at least 60 systems (14%) with values of the σ_{1-2} disagreement greater than 5 where the systematic errors ($\Delta\tau$) are nonnegligible compared to the random errors reported (σ_τ).

4.2. Ill-behaved Systems

Substantial uncertainty in the total ages in these WDs comes from the process of converting the WD mass to a ZAMS progenitor lifetime. We remove the most model-dependent aspect in the determination of the WD's progenitor lifetime by simply considering that the IFMR is monotonic and increasing, such that a higher-mass WD comes from a higher-mass progenitor. This assumption may not hold for all WD masses, as some evidence of a kink is seen in the IFMR for a range of WD masses around $0.65\ M_\odot$ (Marigo et al. 2020).

Still, for the vast majority of cases, the more massive WD in the binary comes from a more massive MS star, and its progenitor lifetime should be smaller than the progenitor

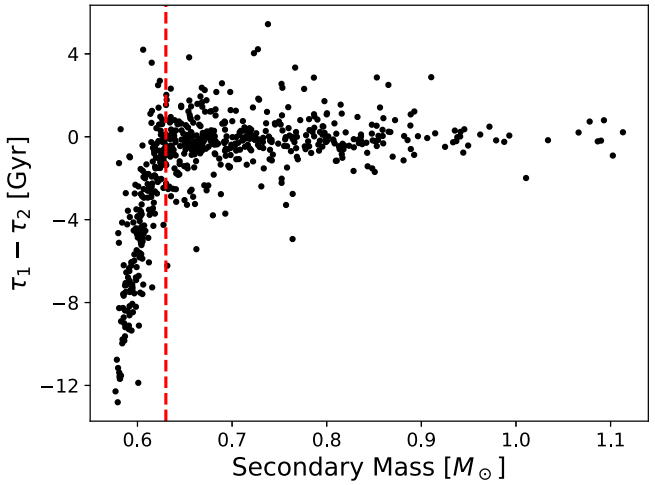

Figure 5. Total age difference in each binary as a function of the mass of the secondary in each binary (the least massive component) for our 1272 systems surviving the cuts outlined in Section 4. The red line shows the cut used to remove the poorly behaved low-mass systems, whose behavior changed drastically at $M < 0.63\ M_\odot$. Since the secondary is always the least massive component, the cut shown by the red line removes all systems with WDs $<0.63\ M_\odot$.

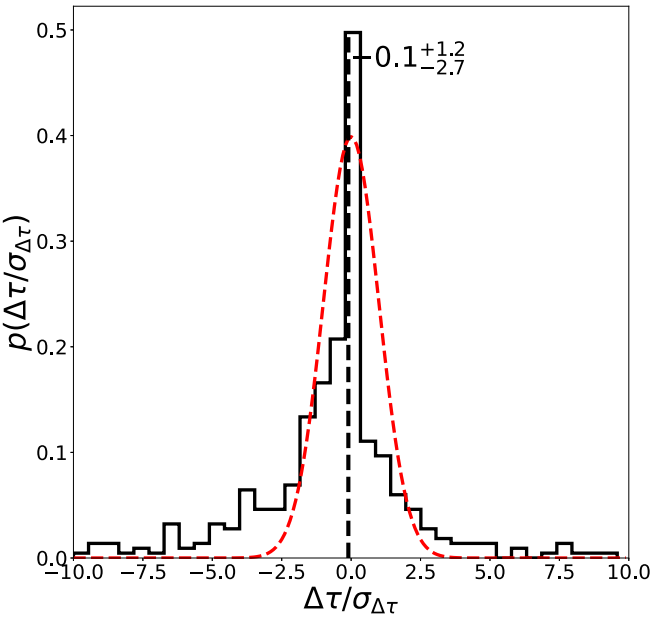

Figure 6. Distribution of σ_{1-2} disagreement for the 423 wide WD+WD pairs in our sample that pass the cuts discussed in Section 4. The red dashed line shows the expected distribution for a Gaussian with $\sigma = 1$ for reference. The distribution is skewed toward negative values, where the primary is the more massive of the two components. The black dashed line represents the 50th percentile, and the lower and upper errors come from the 16th and 84th percentiles, respectively.

lifetime of its companion. For a coeval binary pair, the cooling age of the more massive WD must be longer than the cooling age of its companion. Any systems where the more massive WD has a shorter cooling age than its lower-mass companion are discrepant before invoking any theoretical IFMR or other process for determining a progenitor lifetime.

Our sample contains many systems where this is the case, as shown by Figure 7. The figure includes systems that pass the temperature, separation, and chance alignment cuts discussed in Section 4, but we do not apply the total age and mass cut described in that section for this comparison. Roughly 43% lie in the negative region of the plot, where the more massive WD has a shorter cooling age. This statistic requires that we properly define the more massive WD (see representative uncertainty in Figure 7); 21% of our systems are more than 1σ away from having the more massive component with a shorter cooling age. This is a conservative estimate for the number of these ill-behaved systems because the masses of the two WDs in each pair have a positive correlation. This is due to the fact that the two WDs are effectively at the same distance, and the uncertainty on the distance affects the determined uncertainties on the masses. If in fact the system is closer and therefore brighter, then both WDs would be brighter, and the derived masses would both be lower, leaving the determination of the more massive primary unchanged.

Thus, somewhere between 21% and 43% of the wide WD +WD systems have a more massive WD with a shorter cooling age. Given a monotonic and increasing IFMR, these systems will have large σ_{1-2} disagreement values. The systems that have negative cooling age differences shown in Figure 7 show no bias toward any mass or temperature range. Removal of the 187 ill-behaved systems that pass the cuts described in Section 4 results in a substantial fraction of systems in the long negative tail of the σ_{1-2} disagreement distribution being removed (see Figure 8).

One possible explanation for this discrepancy is that we are assuming that all of our WDs have a hydrogen-dominated atmosphere. Applying a DA (hydrogen-dominated atmosphere) model to a non-DA WD can cause systematic errors on the order of 10%–15% on the WD mass (Giammichele et al. 2012), which can lead to the wrong determination of the primary. The objects in the sample that are known to have two pure DA WDs still show objects in the negative region where the higher-mass WD has a shorter cooling age (see Figure 7). The number of wide DA+DAs that are ill-behaved is around 36% of 74 systems (with 21% being more than 1σ discrepant). Systems where one of the WDs is known from spectroscopy to be a non-DA have 63% out of 73 systems in the negative region (with 52% being more than 1σ discrepant).

Our spectroscopic follow-up using the LDT was designed to specifically target systems in the negative region of Figure 7 and thus biases our results to this region. An alternative way to determine if there is an excess of non-DA systems in the ill-behaved region of Figure 7 without having to worry about the bias introduced by our follow-up observations is to compare the relative rates of the spectral types within the sample of the ill-behaved objects. There are 101 systems in the negative region, and 156 of the 202 WDs have a spectral type determined. Of these WDs, 66% are DAs. In magnitude-limited samples, we expect ≈65% of the WDs to be DAs (Kleinman et al. 2013). For the systems that are more than 1σ discrepant, 59% of the WDs with known spectral types are DAs.

Although there is some evidence for an overabundance of non-DAs in the negative region of Figure 7, we conclude that it is unlikely that a large population of non-DAs is the full explanation for the number of these ill-behaved systems. To avoid any contamination from non-DAs, we will refer to the values for the DA+DA subsample (21%–36%) when discussing the percentage of ill-behaved systems.

Instead, we propose that most of the ill-behaved systems are the descendants of triples that have an inner pair that either

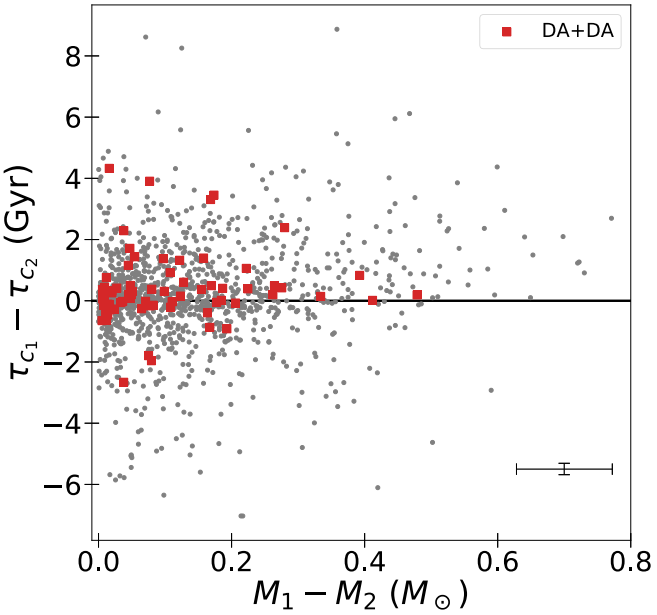

Figure 7. Comparison of the cooling age difference vs. mass difference for the full wide binary sample (1259 gray points) and a subset of pairs where both WDs are known to be DA (79 red squares). A representative error bar is provided in the bottom right corner of the figure. A significant fraction of objects (43% for the full sample, 35% for the DA+DA systems) sit in the negative region, which implies that the more massive component has a shorter cooling age. This is unphysical and likely implies that a large fraction of wide WD+WD binaries were once triple systems.

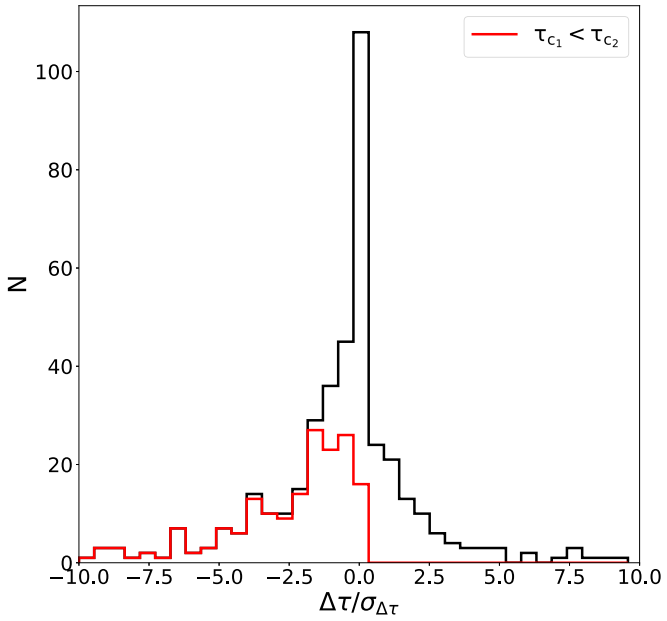

Figure 8. Distribution of the σ_{1-2} disagreement for the 423 wide binaries that pass the cuts outlined in Section 4 (black) compared to the distribution of the σ_{1-2} disagreement for the sample of systems where the more massive WD has a shorter cooling age (red). These systems can account for the bias toward negative values including the most discrepant systems.

experienced a merger that effectively reset the age of the more massive WD or is currently unresolved. Through binary population modeling, Temmink et al. (2020) found that assuming single-star evolution for a merger remnant can result in underestimating the age by three to five times, on average, which could manifest as an anomalous cooling age like those in Figure 7. They also found that 10%−30% of isolated WDs have experienced a merger in their past, usually before the WD phase is reached, which is similar to the percentage of ill-behaved systems in our sample (21%–36%). While that value is for single WDs once in binaries, it is a valuable number to anchor expectations.

If all of the systems in the negative region of Figure 7 are or were previously triples, this implies that roughly 21%–36% of the wide WD+WD pairs in our sample started as a triple system and have either undergone a merger or have a close inner pair that is unresolved. This range is consistent with the expected binary and triple fraction (30%–35% and 10%–20%, respectively) for WD progenitor stars that are 2−4 $M_\odot$ on the ZAMS (Moe & Di Stefano 2017). We also find that 50% of the double WD pairs in the triple systems are in the negative region of Figure 7. This would imply that these systems are descended from quadruple systems.

At least one well-studied merger remnant is included in our sample: the massive (>1.1 $M_\odot$; Külebi et al. 2010), strongly magnetic (up to 800 MG; Burleigh et al. 1999), rapidly rotating (725 s; Vennes et al. 2003) object RE J0317–853 (Ferrario et al. 1997). This WD is in a system with a σ_{1-2} disagreement value of −17, and its effective temperature is at least twice that of its lower-mass companion. We conclude that the majority of these ill-behaved systems are likely merger remnants or unresolved triples. Spectroscopic follow-up of these systems can help to disentangle the subset of these objects that are the result of a merger from the unresolved triples that can place empirical constraints on the triple fraction of WD progenitors.

4.3. Dependence on Mass and Temperature

The dependence of the age disagreement on the WD mass and temperature can provide insights into where our models are insufficient. A treatment and correction for these dependencies is crucial if WD ages are to be used on large scales to age various populations.

We explore the dependence of the age disagreement on the WD mass and temperature by splitting the systems into individual WDs and inspecting the median of the absolute value of the age disagreement of each system in various bins of effective temperature and mass. In this analysis, we do not remove any of the ill-behaved systems discussed in Section 4.2, since it is not usually feasible to separate these possible merger remnants when looking at an isolated WD or WD+MS system in the field.

We find that the age disagreement is effectively constant as a function of temperature but shows a strong trend as a function of mass. This can be seen in Figure 9. The highest masses (>0.8 $M_\odot$) have a median $|\sigma_{1-2}|$ disagreement value of ≈1.5, while the lowest-mass bin (<0.67 $M_\odot$) has a median value of ≈0.6. The uncertainties in the medians shown are found through a bootstrapping method with replacement. To ensure that this trend is the true underlying trend, we calculate the median age disagreement for a subsample of systems where the masses of both WDs in the system are in the same bin. This removes cross-contamination from systems that have WDs with very different masses. The gray points in Figure 9 show the trend for this subsample and are consistent with the points for the whole sample.

This trend in mass can be caused by larger systematic errors in the total ages of massive WDs causing larger relative age differences in the binaries containing them or by an

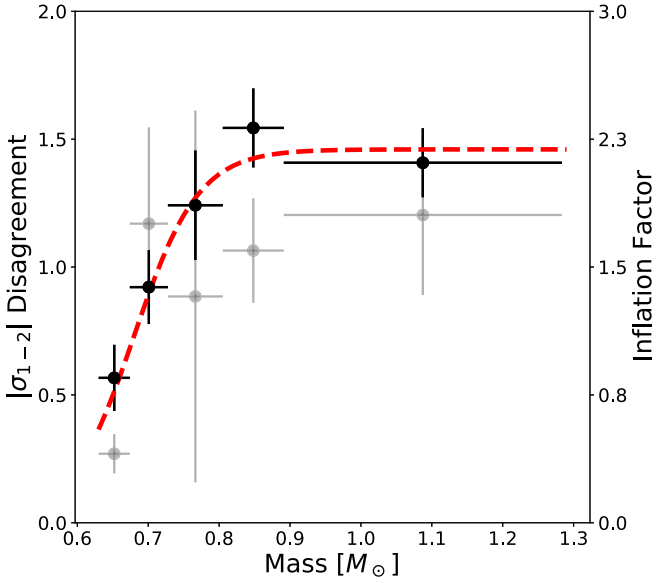

Figure 9. Absolute value of the total age disagreement and the resulting total age error inflation factors as a function of WD mass. Each point represents the median of the absolute value of the total age disagreement of a bin centered at the point. The total age error inflation factors are calculated by dividing this median by the expectation for a folded Gaussian distribution. The black points represent the full sample of 423 systems that survived the cuts described in Section 4. The gray background points represent the median age disagreement for a subsample of systems where both WDs have masses contained in each bin. Each bin contains 20% of the sample, which is roughly 170 individual WDs per bin for the black points (the gray points are around three to five times fewer). The red line is a fit to the black points that is described in Section 4.3 to define an inflation factor; a coarse mapping for this fit can be found in Table 1.

underestimation of the total age uncertainties of high-mass WDs. We find that the relative age difference is essentially constant (≈25%) as a function of WD mass. This leads us to conclude that the uncertainties on the total ages of the high-mass WDs in the sample are underestimated.

To determine the amount of inflation of the total age errors needed, we take the median age disagreement and divide by the expected median value of a folded Gaussian distribution with a standard deviation of 1. These values can be seen as a second y-axis in Figure 9. Next, we fit these points with a sigmoid function, defined as

$$f_{\rm inflate}(M_\odot) = \frac{a}{1 + {\rm e}^{-c(M-b)}}, \quad (3)$$

where M is the mass of the WD, and a, b, and c are all constants. We fit this function to the inflation factor points shown in Figure 9. The best-fit parameters are $a = 2.2$, $b = 0.68$, and $c = 22$. The resultant fit can be seen in Figure 9 as the red dashed line, and select points are given in Table 1. The total age error inflation factor for the lowest-mass bin is 0.85, but we do not recommend deflating any total age errors. The uncertainty makes the point consistent with a total age error inflation factor of 1.0. Thus, we recommend using the fit function only for WDs with masses greater than 0.67 $M_\odot$.

To further understand where WD ages are the most reliable, we split the parameter space into 25 bins in temperature and mass. For each bin, we check the median total age, absolute age difference, and total age error inflation factor needed. The results of this are shown in Figure 10. The most problematic areas of parameter space are the higher masses, which is what

Table 1
Total Age Error Inflation Factors

WD Mass [$M_\odot$]	$f_{\rm inflate}$	WD Mass [$M_\odot$]	$f_{\rm inflate}$
0.67	1.00	0.74	1.74
0.68	1.10	0.75	1.81
0.69	1.20	0.76	1.88
0.70	1.34	0.77	1.90
0.71	1.45	0.78	2.00
0.72	1.55	0.80	2.05
0.73	1.65	>0.90	2.20

is seen in Figure 9, especially at the hotter temperatures, where the cooling age contribution to the total age is minimized. These hot, high-mass regions of parameter space are where we would expect the merger remnants to be at their highest contamination rate. This is also where the Q-branch is located, which was first seen in the H-R diagram in Gaia DR2 (Gaia Collaboration et al. 2018b; Cheng et al. 2019), as well as the onset of crystallization (Tremblay et al. 2019). The cooling models we use do include crystallization but not other exotic cooling effects, such as sedimentation of neutron-rich ions (e.g., Bildsten & Hall 2001; Bauer et al. 2020; Blouin et al. 2021).

The typical percent age difference across all of the bins is around 25%, ranging from 60% in the worst case ($T_{\rm eff} >$ 12,000 K, 0.8 $M_\odot < M <$ 0.9 $M_\odot$) to 15% in the best case (7550 K $< T_{\rm eff} <$ 9100 K, 0.73 $M_\odot < M <$ 0.8 $M_\odot$). The WDs with the hottest temperatures show larger percent age differences on the order of 35%–60% (0.2–0.5 Gyr) compared to the rest of the parameter space. Thus, 25% total age uncertainties are a representative approximation for most WD age estimates on an individual WD for WDs >0.63 $M_\odot$ and temperatures cooler than 12,000 K. This median WD age precision compares well to similar results from an independent analysis of many of the same objects (Qiu et al. 2021). It should be noted that with additional information through spectroscopy, we can achieve better age precision (Moss et al. 2022).

5. Conclusions

In this work, we constructed a sample of 1565 wide WD+WD binaries, as well as 24 mostly new wide triple WD +WD+X systems, to test the accuracy and precision of WD total age determinations when no spectral type information is known. We measured effective temperatures, surface gravities, and masses for all WDs in our sample by using hydrogen-dominated atmosphere models and fitting photometry from a variety of all-sky surveys. Using these atmospheric parameters, we determined the total ages of each WD through the use of WD cooling models, a theoretically motivated and observationally calibrated IFMR, and stellar evolution model grids.

Using a high-fidelity sample of wide WD+WD pairs with uncontaminated photometry described in Section 4, the main conclusions of this work can be summarized as follows.

1. We find 24 mostly new widely separated triples with at least two WDs and possibly the second ever resolved triple WD system. We find that 21 of the 24 triples have a hierarchical structure. The three triples not in a hierarchical structure will likely dissipate due to dynamical instability, but the ages of the WDs in these systems can provide useful lower limits on the dissipation

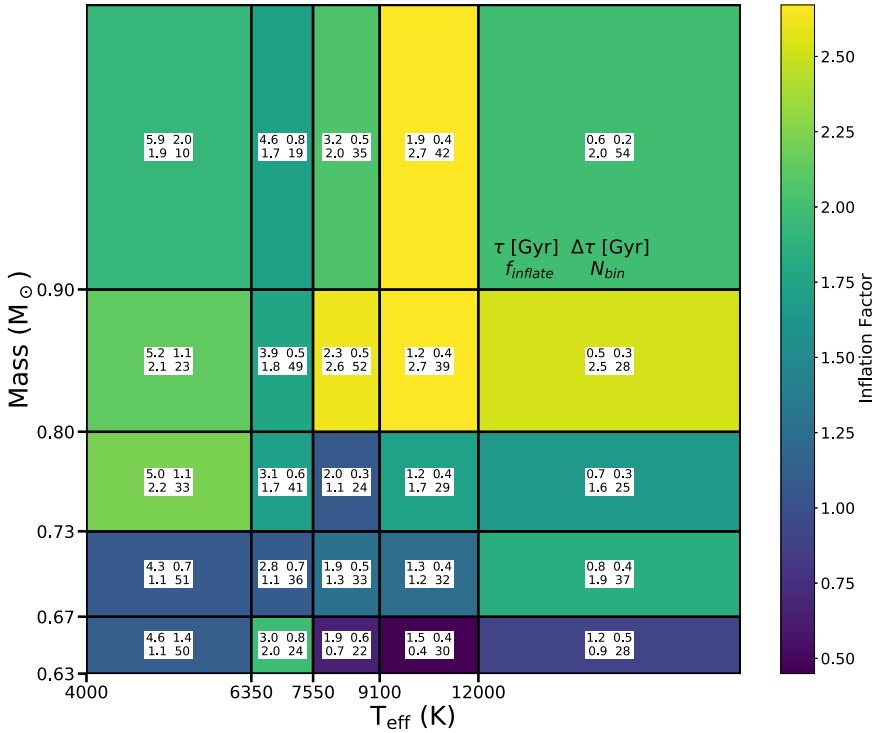

Figure 10. Inflation factor and median total age and age difference for 25 bins in mass and temperature of roughly similar size. Each box is colored by the inflation factor, and the white box shows the median total age (gigayears; upper left), median total age difference (gigayears; upper right), total age error inflation factor (lower left), and number of WDs in the bin (lower right). The upper right bin also includes the parameters represented in the white boxes. For example, the 50 WDs in the bottom left bin (4000–6350 K, 0.63–0.67 $M_\odot$) have a median total age of 4.6 Gyr, their ages differ from their companions by 1.4 Gyr on average, and their total age uncertainties need to be inflated by a factor of 1.2 for their ages to come into 1σ agreement.

timescale. We find that two of the nonheirarchical triple systems are ≈3 Gyr old, while the other is quite young at ≈90 Myr old.

2. We find that the total ages of the lowest-mass WDs in the sample (<0.63 $M_\odot$) are too uncertain to be used in the age comparisons conducted in this work. The absolute age difference of systems containing at least one lower-mass WD quickly diverges toward high values of a few gigayears. A lower limit on the total age can still be determined for these WDs, but we do not attempt to test the absolute reliability of their total ages. This is unfortunate, since the mean mass of field WDs is roughly 0.63 $M_\odot$ (Kepler et al. 2016; Tremblay et al. 2016; Kepler et al. 2019).
3. When comparing the total ages of each component of the WD pairs, we find a significant fraction of systems (21%–43%) where the more massive WD has a shorter cooling age. We find that this trend holds even for a subsample of DA+DA systems, with 21%–36% having the more massive WD with a shorter cooling age. This is the opposite of what is expected for a monotonic and increasing IFMR. We attribute this discrepancy to the presence of many merger remnants or unresolved triples in the sample, such that roughly 21%−36% of our sample of currently wide WD+WD binaries started as bound triple systems. These WDs have large age disagreement values and can cause problems when determining ages for field WDs, but unresolved companions or a merger history is a problem for many techniques for determining stellar ages.
4. We find that the level of age disagreement strongly depends on the mass of the WD. Wide binaries containing at least one higher-mass WD (>0.8 $M_\odot$) generally have a lower level of agreement compared to those with lower-mass WDs, reflecting the fact that the formal age uncertainties are often underestimated for higher-mass WDs. We fit this dependence to determine the amount of error inflation on the total ages needed to improve the agreement. We find that errors on the total ages of the highest-mass WDs (>0.9 $M_\odot$) need to be inflated, up to a factor of 2.2, when assuming that the WD is a DA. Fortunately, higher-mass WDs also have more precisely determined ages (median total age uncertainties of ≈0.2 Gyr), so they remain very useful chronometers.
5. Looking at 25 bins in mass and effective temperature space in Figure 9, we find that the total ages are roughly accurate at the 25% level for WDs with masses >0.63 $M_\odot$ using only photometry. The WDs with the hottest temperatures have the largest inaccuracy, with uncertainties of 35%–60%, but these are relatively small absolute errors on the order of 0.3 Gyr.

Due to the large sample size, we assumed that all of the WDs in our sample are DA. When a spectral type is known, a more accurate total age can be determined, and the recommendations discussed above are not immediately applicable. A large sample of wide double WDs with known spectral types needs to be investigated to determine the accuracy of the total ages of WDs when the spectral type is known.

Future work is planned to quantify how atmospheric parameters from spectroscopy can alleviate the systematic errors mentioned above. Spectroscopic observations do not suffer from the same problems as the photometric methods employed in this work and should be more sensitive to the WD

mass. A spectrum can also provide important clues as to whether a WD has a prior merger history or is part of an unresolved binary (for example, if it is strongly magnetic or radial velocity variable). With our follow-up efforts using the LDT, we continue to increase the sample of wide WD+WD pairs with available spectra in hopes of gathering a large sample of wide double WDs with spectroscopically determined atmospheric parameters.

In general, we find that the total ages of WDs agree very well in wide double WDs, but the uncertainties occasionally need to be inflated to compensate for systematics on the total ages, the presence of an unresolved companion, or merger history. Given the massive increase in the number of systems with a wide WD companion thanks to Gaia, we hope this result provides a first road map to providing more reliable stellar ages using these wide binaries.

We acknowledge helpful comments from the anonymous referee. We would like to acknowledge Jeff Andrews for helpful discussions. T.M.H., J.J.H., and C.W. acknowledge support from the National Science Foundation under grant No. AST-1908119. J.v.S. acknowledges support from the National Science Foundation under grant No. AST-1908723. We thank Phil Muirhead and Adam Samuels for support with the quick-look spectroscopic tool.

This work has made use of data from the European Space Agency (ESA) mission Gaia (https://www.cosmos.esa.int/gaia), processed by the Gaia Data Processing and Analysis Consortium (DPAC; https://www.cosmos.esa.int/web/gaia/dpac/consortium). Funding for the DPAC has been provided by national institutions, in particular the institutions participating in the Gaia Multilateral Agreement. These results made use of the Lowell Discovery Telescope (LDT) at Lowell Observatory. Lowell is a private, nonprofit institution dedicated to astrophysical research and public appreciation of astronomy and operates the LDT in partnership with Boston University, the University of Maryland, the University of Toledo, Northern Arizona University, and Yale University. The upgrade of the DeVeny optical spectrograph has been funded by a generous grant from John and Ginger Giovale and a grant from the Mt. Cuba Astronomical Foundation.

Appendix A
Double WD Pair Catalog and Triples Catalog

The full catalog of wide double WD pairs with total ages and atmospheric parameters can be found as supplemental material. Table A1 gives a description of the columns of the catalog. Table A2 shows the 23 WD+WD+MS and WD+WD+WD triples found in this work.

Table A1
Double WD Pair Catalog Description

Column	Units	Description
ID		Name of the system; determined by the source_id of the brightest component
GaiaP		Gaia EDR3 source identifier
RAdegP	deg	R.A. (J2016)
DEdegP	deg	Decl. (J2016)
pmRAP	mas yr^{-1}	Proper motion in the direction of R.A.
e_pmRAP	mas yr^{-1}	Uncertainty on the proper motion in the direction of R.A.
pmDEP	mas yr^{-1}	Proper motion in the direction of decl.
e_pmDEP	mas yr^{-1}	Uncertainty on the proper motion in the direction of decl.
plxP	mas	Parallax
e_plxP	mas	Uncertainty on the parallax
GmagP	mag	Gaia EDR3 G-band magnitude
GFluxP	e$^-$ s^{-1}	Gaia EDR3 G-band flux
e_GFluxP	e$^-$ s^{-1}	Uncertainty on the Gaia EDR3 G-band flux
BpmagP	mag	Gaia EDR3 G_{BP}-band magnitude
BpFluxP	e$^-$ s^{-1}	Gaia EDR3 G_{BP}-band flux
e_BpFluxP	e$^-$ s^{-1}	Uncertainty on the Gaia EDR3 G_{BP}-band flux
RpmagP	mag	Gaia EDR3 G_{RP}-band magnitude
RpFluxP	e$^-$ s^{-1}	Gaia EDR3 G-band flux
e_RpFluxP	e$^-$ s^{-1}	Uncertainty on the Gaia EDR3 G_{RP}-band flux
uSDSSmagP	mag	SDSS u-band magnitude
gSDSSmagP	mag	SDSS g-band magnitude
rSDSSmagP	mag	SDSS r-band magnitude
iSDSSmagP	mag	SDSS i-band magnitude
zSDSSmagP	mag	SDSS z-band magnitude
e_uSDSSmagP	mag	Uncertainty on the SDSS u-band magnitude
e_gSDSSmagP	mag	Uncertainty on the SDSS g-band magnitude
e_rSDSSmagP	mag	Uncertainty on the SDSS r-band magnitude
e_iSDSSmagP	mag	Uncertainty on the SDSS i-band magnitude
e_zSDSSmagP	mag	Uncertainty on the SDSS z-band magnitude
uSMAPmagP	mag	SkyMapper u-band magnitude
vSMAPmagP	mag	SkyMapper v-band magnitude
gSMAPmagP	mag	SkyMapper g-band magnitude
rSMAPmagP	mag	SkyMapper r-band magnitude
iSMAPmagP	mag	SkyMapper i-band magnitude
zSMAPmagP	mag	SkyMapper z-band magnitude
e_uSMAPmagP	mag	Uncertainty on the SkyMapper u-band magnitude
e_vSMAPmagP	mag	Uncertainty on the SkyMapper v-band magnitude
e_gSMAPmagP	mag	Uncertainty on the SkyMapper g-band magnitude
e_rSMAPmagP	mag	Uncertainty on the SkyMapper r-band magnitude
e_iSMAPmagP	mag	Uncertainty on the SkyMapper i-band magnitude
e_zSMAPmagP	mag	Uncertainty on the SkyMapper z-band magnitude
gPSTRmagP	mag	PanSTARRS g-band magnitude
rPSTRmagP	mag	PanSTARRS r-band magnitude
iPSTRmagP	mag	PanSTARRS i-band magnitude
zPSTRmagP	mag	PanSTARRS z-band magnitude
yPSTRmagP	mag	PanSTARRS y-band magnitude
e_gPSTRmagP	mag	Uncertainty on the PanSTARRS g-band magnitude
e_rPSTRmagP	mag	Uncertainty on the PanSTARRS r-band magnitude
e_iPSTRmagP	mag	Uncertainty on the PanSTARRS i-band magnitude
e_zPSTRmagP	mag	Uncertainty on the PanSTARRS z-band magnitude
e_yPSTRmagP	mag	Uncertainty on the PanSTARRS y-band magnitude
JmagP	mag	2MASS J-band magnitude
HmagP	mag	2MASS H-band magnitude
KmagP	mag	2MASS Ks-band magnitude
e_JmagP	mag	Uncertainty on the 2MASS J-band magnitude
e_HmagP	mag	Uncertainty on the 2MASS H-band magnitude
e_KmagP	mag	Uncertainty on the 2MASS Ks-band magnitude
log(g)P	[cm s^{-2}]	Log of the surface gravity from a DA model with a thick H layer
E_log(g)P	[cm s^{-2}]	Upper uncertainty on the log of the surface gravity from a DA model
e_log(g)P	[cm s^{-2}]	Lower uncertainty on the log of the surface gravity from a DA model
TeffP	K	Effective temperature from a DA model
E_TeffP	K	Upper uncertainty on the effective temperature from a DA model
e_TeffP	K	Lower uncertainty on the effective temperature from a DA model
MP	$M_\odot$	Mass from a DA model
E_MP	$M_\odot$	Upper uncertainty on the mass from a DA model
e_MP	$M_\odot$	Lower uncertainty on the mass from a DA model
CAgeP	Gyr	Cooling age for a DA model
E_CAgeP	Gyr	Upper uncertainty on the cooling age for a DA model
e_CAgeP	Gyr	Lower uncertainty on the cooling age for a DA model
iMP	$M_\odot$	Initial ZAMS mass
E_iMP	$M_\odot$	Upper uncertainty on the initial mass
e_iMP	$M_\odot$	Lower uncertainty on the initial mass
TAgeP	Gyr	Total age of the WD
E_TAgeP	Gyr	Upper uncertainty on the total age
e_TAgeP	Gyr	Lower uncertainty on the total age
SpTypeP		Spectral type of the WD, if available
SpTypeS		Source of spectral type[a]
plxW	mas	Weighted mean of the parallax of the system
e_plxW	mas	Uncertainty on the weighted mean of the parallax of the system
Sep	au	Projected on-sky separation for the pair
Chance		Chance alignment variable from El-Badry et al. (2021)

Notes. Columns dealing with properties of the individual WDs will have "_P" or "_S" at the end to denote the primary and secondary, respectively, where the primary has been defined as the more massive WD. The final 26 rows contain the wide double WD pairs from the triples found in this paper.

[a] Spectral types in this work are collected from Sion et al. (1991), Finley & Koester (1997), McCook & Sion (1999), Croom et al. (2004), Koester et al. (2009), Külebi et al. (2010), Tremblay et al. (2011), Bergeron et al. (2011), Gianninas et al. (2011), Dobbie et al. (2012), Kleinman et al. (2013), Limoges et al. (2013), Baxter et al. (2014), Andrews et al. (2015), Kepler et al. (2015), Ferrario et al. (2015), Guo et al. (2015), Kepler et al. (2016), Gentile Fusillo et al. (2019), Kilic et al. (2020), and Tremblay et al. (2020).

(This table is available in machine-readable form.)

Table A2
WD+WD+X Triples

System Name	Source_id (EDR3)	R.A. (J2016°)	Decl. (J2016°)	$\mu_{\mathrm{R.A.}}$ (mas yr^{-1})	$\mu_{\mathrm{decl.}}$ (mas yr^{-1})	ω (mas)	G (mag)	Stellar Type	θ_{12} (au)	θ_{13} (au)	θ_{23} (au)
WDWDMS	105617338913173888	30.6841382	26.0846896	-21.52 ± 0.08	9.97 ± 0.08	3.75 ± 0.08	15.4	MS			
EDR3	105617304552984576	30.6768988	26.0867710	-21.55 ± 0.39	9.83 ± 0.38	3.93 ± 0.34	19.4	WD	6550	6330	386
105617338913173888	105617338913173760	30.6772592	26.0870098	-21.64 ± 0.48	9.80 ± 0.44	3.56 ± 0.38	19.5	WD			
WDWDMS	1463032750563461248	198.5937866	30.8450953	-47.76 ± 0.01	26.49 ± 0.01	7.17 ± 0.02	11.9	MS			
EDR3	1463032819282938112	198.5894261	30.8474817	-48.30 ± 0.09	27.43 ± 0.08	7.16 ± 0.11	17.8	WD	2230	2010	385
1463032750563461248	1463032819282938240	198.5902718	30.8477281	-48.02 ± 0.11	25.96 ± 0.10	7.26 ± 0.14	18.1	WD			
WDWDMS	1932475596596345088	340.4531174	40.4721954	47.54 ± 0.01	140.41 ± 0.01	12.50 ± 0.01	12.4	MS			
EDR3	1932475596593097344	340.4527195	40.4734028	43.98 ± 0.08	141.16 ± 0.09	12.41 ± 0.10	17.6	WD	359	5380	5340
1932475596596345088	1932475562233361536	340.4758520	40.4792377	45.46 ± 0.15	140.12 ± 0.19	12.55 ± 0.21	18.9	WD			
WDWDMS	2063683029262340608	311.2472539	39.4521779	-18.82 ± 0.17	-34.76 ± 0.20	5.74 ± 0.17	18.9	MS			
EDR3	2063684201794288512	311.1961772	39.5036734	-18.42 ± 0.21	-34.48 ± 0.23	5.25 ± 0.20	19.2	WD	43,200	43,400	400
2063683029262340608	2063684201788243712	311.1954031	39.5037395	-18.65 ± 0.23	-35.06 ± 0.26	5.06 ± 0.22	19.4	WD			
WDWDMS	2477316902742801152	22.1010462	−8.3944721	-60.79 ± 0.02	-170.47 ± 0.01	9.41 ± 0.02	9.2	MS			
EDR3	2477317211979980544	22.1036359	−8.3822745	−62.28 0.31	-171.74 ± 0.16	10.75 ± 0.28	18.6	WD	4765	4879	128
2477316902742801152	2477317211980446208	22.1038481	−8.3820147	-61.01 ± 0.86	-170.16 ± 0.17	9.74 ± 0.39	18.8	WD			
WDWDMS	3197507047683918976	61.4674880	−5.3325341	15.68 ± 0.54	-21.82 ± 0.57	3.95 ± 0.59	20.1	WD			
EDR3	3197506983261219328	61.4666405	−5.3345423	17.00 ± 0.74	-22.07 ± 0.65	5.79 ± 0.77	20.3	WD	1700	18,000	17,000
3197507047683918976	3197506944605295488	61.4588283	−5.3547354	15.25 ± 0.78	-22.32 ± 0.73	4.70 ± 0.85	20.5	MS			
WDWDMS	3218914298562400640	88.5970332	0.6795522	-3.25 ± 0.22	-12.71 ± 0.19	3.64 ± 0.22	18.8	WD			
EDR3	3218914298560464768	88.5960159	0.6820507	-3.39 ± 0.45	-12.21 ± 0.39	4.50 ± 0.45	19.7	WD	2600	36,000	38,000
3218914298562400640	3218912889811507072	88.6192839	0.6487874	-2.52 ± 0.48	-12.21 ± 0.41	3.78 ± 0.49	19.7	MS			
WDWDMS	3389527411923077376	82.8666421	13.4102532	56.74 ± 0.02	-19.96 ± 0.01	6.29 ± 0.02	9.3	MS			
EDR3	3389527338906751744	82.8642176	13.3994875	56.72 ± 0.52	-19.40 ± 0.33	6.70 ± 0.49	19.9	WD	6300	6690	390
3389527411923077376	3389527343202017280	82.8640568	13.3988239	55.58 ± 0.65	-19.04 ± 0.40	6.33 ± 0.59	20.1	WD			
WDWDMS	338979267341825408	35.0462274	41.0692488	16.16 ± 0.02	-43.19 ± 0.02	6.11 ± 0.02	13.1	MS			
EDR3	338979301700437120	35.0674487	41.0816494	16.58 ± 0.71	-44.35 ± 0.68	6.91 ± 0.57	20.1	WD	11,920	12,370	460
338979267341825408	338979297405358848	35.0681580	41.0822196	15.83 ± 0.94	-44.05 ± 0.88	5.67 ± 0.72	20.4	WD			
WDWDMS	3681220906103896192	188.0529329	−4.1563234	-150.63 ± 0.02	0.21 ± 0.02	11.30 ± 0.02	8.8	MS			
EDR3	3681220906102862720	188.0547401	−4.1571420	-153.55 ± 0.07	1.45 ± 0.06	11.35 ± 0.07	15.7	WD	630	750	208
3681220906103896192	3681220906103896064	188.0547785	−4.1577956	-151.04 ± 0.06	3.74 ± 0.05	11.33 ± 0.06	15.7	WD			
WDWDMS	4438147044497125248	243.7861861	6.3673258	-55.58 ± 0.05	21.32 ± 0.04	3.82 ± 0.06	16.2	MS			
EDR3	4438147418158270848	243.7956106	6.3658639	-55.44 ± 0.65	20.13 ± 0.52	3.41 ± 0.61	20.2	WD	8900	9500	554
4438147044497125248	4438147422454430464	243.7961101	6.3655519	-54.09 ± 0.81	20.39 ± 0.60	3.74 ± 0.66	20.4	WD			
WDWDMS	4987518647789031040	13.6994498	−40.0797643	10.22 ± 0.01	32.19 ± 0.01	5.27 ± 0.01	12.8	MS			
EDR3	4987518682147617024	13.6869636	−40.0802902	10.16 ± 0.42	31.98 ± 0.49	5.93 ± 0.51	20.2	WD	6540	6390	285
4987518647789031040	4987518682148769280	13.6872776	−40.0806311	10.64 ± 0.53	32.40 ± 0.68	5.08 ± 0.69	20.5	WD			
WDWDMS	5041268170632888704	20.2704431	−23.8818893	81.43 ± 0.02	-84.14 ± 0.01	8.48 ± 0.02	14.1	MS			
EDR3	5041268200697001600	20.2798805	−23.8794056	82.22 ± 0.45	-83.36 ± 0.33	9.04 ± 0.41	19.8	WD	3810	4080	278
5041268170632888704	5041268204992049664	20.2805981	−23.8793989	82.86 ± 0.64	-85.21 ± 0.46	8.88 ± 0.62	20.3	WD			

Table A2
(Continued)

System Name	Source_id (EDR3)	R.A. (J2016°)	Decl. (J2016°)	$\mu_{\mathrm{R.A.}}$ (mas yr^{-1})	$\mu_{\mathrm{decl.}}$ (mas yr^{-1})	ω (mas)	G (mag)	Stellar Type	θ_{12} (au)	θ_{13} (au)	θ_{23} (au)
WDWDMS	5250998123862710272	143.2102271	−61.9153951	91.80 ± 0.07	−118.74 ± 0.05	8.43 ± 0.04	16.4	MS			
EDR3	5250998119556563200	143.2106552	−61.9129685	92.89 ± 0.23	−117.90 ± 0.15	8.54 ± 0.14	18.9	WD	1038	18,650	17,670
5250998123862710272	5251022416193428096	143.1869479	−61.8730341	92.32 ± 0.69	−117.36 ± 0.47	8.89 ± 0.41	20.2	WD			
WDWDMS	5455352324194328192	158.0412243	−29.9751592	72.86 ± 0.01	−5.94 ± 0.02	7.89 ± 0.02	10.5	MS			
EDR3	5455352702151342592	158.0283938	−29.9535991	72.95 ± 0.06	−6.34 ± 0.10	7.78 ± 0.10	17.4	WD	11,080	10,020	1077
5455352324194328192	5455352697853121280	158.0291298	−29.9558703	73.17 ± 0.23	−5.65 ± 0.41	7.42 ± 0.41	19.7	WD			
WDWDMS	5560517931332969600	111.8889790	−41.3676372	−154.05 ± 0.01	−4.86 ± 0.01	9.65 ± 0.01	11.5	MS			
EDR3	5560518000052459520	111.9127938	−41.3679211	−153.72 ± 0.06	−5.43 ± 0.06	9.61 ± 0.06	17.1	WD	6671	6676	559
5560517931332969600	5560518000048274304	111.9127590	−41.3664248	−153.02 ± 0.79	−6.17 ± 0.91	9.91 ± 0.76	20.5	WD			
WDWDMS	5874024705460836992	224.4952433	−63.2877651	−33.67 ± 0.02	−54.39 ± 0.02	8.60 ± 0.02	8.1	MS			
EDR3	5874024769842933760	224.5481622	−63.2928712	−34.04 ± 0.06	−54.37 ± 0.06	8.49 ± 0.06	16.8	WD	10,190	10,440	299
5874024705460836992	5874024774146311808	224.5496572	−63.2926298	−33.33 ± 0.09	−53.16 ± 0.09	8.75 ± 0.09	17.5	WD			
WDWDMS	6087696442178470400	202.4274557	−44.0483557	−14.23 ± 0.08	−5.96 ± 0.06	3.89 ± 0.07	16.8	MS			
EDR3	6087695613244135936	202.4327137	−44.0750059	−14.20 ± 0.20	−6.22 ± 0.17	3.48 ± 0.21	18.9	WD	25,200	25,800	840
6087696442178470400	6087695617537911040	202.4318915	−44.0756854	−15.18 ± 0.33	−5.69 ± 0.26	3.53 ± 0.31	19.6	WD			
WDWDMS	6145125411962111104	184.8137056	−42.3393993	−25.88 ± 0.02	9.91 ± 0.02	2.88 ± 0.03	15.4	MS			
EDR3	6145125411959049856	184.8084702	−42.3439378	−25.86 ± 0.26	10.15 ± 0.20	3.35 ± 0.32	19.5	WD	7450	7930	482
6145125411962111104	6145125411962108416	184.8080984	−42.3442087	−25.93 ± 0.34	9.64 ± 0.31	3.03 ± 0.48	19.7	WD			
WDWDMS	6756233901661753472	288.8382875	−32.3347021	15.70 ± 0.02	4.10 ± 0.01	6.05 ± 0.02	11.8	MS			
EDR3	6756233905958975360	288.8369795	−32.3330247	15.28 ± 0.36	4.63 ± 0.29	6.67 ± 0.34	19.4	WD	1195	2191	1757
6756233901661753472	6756233905958976512	288.8339392	−32.3344810	16.28 ± 0.52	2.76 ± 0.44	5.71 ± 0.47	19.9	WD			
WDWDMS	763543514763336832	169.8371661	37.0721947	90.75 ± 0.01	−53.81 ± 0.02	8.82 ± 0.02	12.0	MS			
EDR3	763543312899793664	169.8497518	37.0715253	90.80 ± 0.48	−54.38 ± 0.58	9.27 ± 0.51	19.8	WD	4108	3937	423
763543514763336832	763543308609191936	169.8490934	37.0706329	89.68 ± 0.48	−54.14 ± 0.59	8.93 ± 0.50	19.9	WD			
WDWDMS	779305808516516864	161.4150757	40.0952785	−72.91 ± 0.03	21.17 ± 0.03	6.99 ± 0.03	14.9	MS			
EDR3	779305808516517376	161.4055376	40.0933527	−74.03 ± 0.22	21.61 ± 0.25	7.23 ± 0.27	18.8	WD	3880	4050	183
779305808516516864	779305808516231552	161.4050805	40.0934117	−71.23 ± 0.25	21.35 ± 0.24	7.36 ± 0.29	18.9	WD			
WDWDMS	929001808377561216	121.6861312	44.7481737	3.01 ± 0.03	−3.41 ± 0.03	4.99 ± 0.03	15.5	MS			
EDR3	929001804082135168	121.6837451	44.7508697	3.08 ± 0.15	−3.38 ± 0.11	4.93 ± 0.14	18.2	WD	2230	2710	1023
929001808377561216	929001804082135296	121.6818686	44.7503870	3.46 ± 0.21	−2.99 ± 0.16	5.00 ± 0.20	18.8	WD			
WDWDWD	4190499986125543168	298.3999651	−10.3254921	−11.48 ± 0.07	−16.52 ± 0.04	7.75 ± 0.06	16.3	WD			
EDR3	4190499986125543296	298.4001112	−10.3248602	−10.92 ± 0.07	−15.78 ± 0.04	7.66 ± 0.06	16.4	WD	302	6280	6490
4190499986125543168	4190500054845023488	298.3879711	−10.3319738	−10.96 ± 0.11	−16.14 ± 0.06	7.76 ± 0.10	17.3	WD			

Appendix B
Shifted IFMR

The table used for the IFMR in Figure 3 is detailed here in Table B1, adapted from Fields et al. (2016). The WD mass is M_f, and the ZAMS mass is M_i.

Table B1
Shifted MESA IFMR

M_i [$M_\odot$]	M_f [$M_\odot$]	M_i [$M_\odot$]	M_f [$M_\odot$]
1.0	0.583	3.5	0.802
1.1	0.594	3.6	0.828
1.2	0.601	3.7	0.848
1.3	0.608	3.8	0.868
1.4	0.613	3.9	0.880
1.5	0.615	4.0	0.888
1.6	0.619	4.1	0.895
1.7	0.621	4.2	0.901
1.8	0.624	4.3	0.906
1.9	0.625	4.4	0.913
2.0	0.629	4.5	0.919
2.1	0.634	4.6	0.927
2.2	0.640	4.7	0.930
2.3	0.645	4.8	0.939
2.4	0.651	4.9	0.955
2.5	0.657	5.0	0.960
2.6	0.664	5.1	0.957
2.7	0.672	5.2	0.965
2.8	0.682	5.3	0.974
2.9	0.697	5.4	0.983
3.0	0.709	5.5	0.994
3.1	0.724	5.6	1.006
3.2	0.743	5.7	1.020
3.3	0.763	5.9	1.023
3.4	0.780	6.0	1.033

ORCID iDs

Tyler M. Heintz https://orcid.org/0000-0003-3868-1123
J. J. Hermes https://orcid.org/0000-0001-5941-2286
Kareem El-Badry https://orcid.org/0000-0002-6871-1752
Jennifer L. van Saders https://orcid.org/0000-0002-4284-8638
C. E. Fields https://orcid.org/0000-0002-8925-057X
Detlev Koester https://orcid.org/0000-0002-6164-6978

References

Andrews, J. J., Agüeros, M. A., Gianninas, A., et al. 2015, ApJ, 815, 63
Astropy Collaboration, Price-Whelan, A. M., Sipőcz, B. M., et al. 2018, AJ, 156, 123
Barrientos, M., & Chanamé, J. 2021, ApJ, 923, 181
Bauer, E. B., Schwab, J., Bildsten, L., & Cheng, S. 2020, ApJ, 902, 93
Baxter, R. B., Dobbie, P. D., Parker, Q. A., et al. 2014, MNRAS, 440, 3184
Bédard, A., Bergeron, P., Brassard, P., & Fontaine, G. 2020, ApJ, 901, 93
Bergeron, P., Dufour, P., Fontaine, G., et al. 2019, ApJ, 876, 67
Bergeron, P., Wesemael, F., & Beauchamp, A. 1995, PASP, 107, 1047
Bergeron, P., Wesemael, F., Dufour, P., et al. 2011, ApJ, 737, 28
Bida, T. A., Dunham, E. W., Massey, P., & Roe, H. G. 2014, Proc. SPIE, 9147, 91472N
Bildsten, L., & Hall, D. M. 2001, ApJL, 549, L219
Blouin, S., Daligault, J., & Saumon, D. 2021, ApJL, 911, L5
Bressan, A., Marigo, P., Girardi, L., et al. 2012, MNRAS, 427, 127
Burleigh, M. R., Jordan, S., & Schweizer, W. 1999, ApJL, 510, L37
Catalán, S., Isern, J., García-Berro, E., & Ribas, I. 2008, MNRAS, 387, 1693
Cheng, S., Cummings, J. D., & Ménard, B. 2019, ApJ, 886, 100
Choi, J., Dotter, A., Conroy, C., et al. 2016, ApJ, 823, 102
Croom, S. M., Smith, R. J., Boyle, B. J., et al. 2004, MNRAS, 349, 1397
Cummings, J. D., Kalirai, J. S., Choi, J., et al. 2019, ApJL, 871, L18
Cummings, J. D., Kalirai, J. S., Tremblay, P. E., & Ramirez-Ruiz, E. 2015, ApJ, 807, 90
Cummings, J. D., Kalirai, J. S., Tremblay, P. E., & Ramirez-Ruiz, E. 2016, ApJ, 818, 84
Cummings, J. D., Kalirai, J. S., Tremblay, P. E., Ramirez-Ruiz, E., & Choi, J. 2018, ApJ, 866, 21
deBoer, R. J., Görres, J., Wiescher, M., et al. 2017, RvMP, 89, 035007
Dobbie, P. D., Baxter, R., Külebi, B., et al. 2012, MNRAS, 421, 202
Doherty, C. L., Gil-Pons, P., Siess, L., Lattanzio, J. C., & Lau, H. H. B. 2015, MNRAS, 446, 2599
Dotter, A. 2016, ApJS, 222, 8
Eisenstein, D. J., Liebert, J., Koester, D., et al. 2006, AJ, 132, 676
El-Badry, K., & Rix, H.-W. 2018, MNRAS, 480, 4884
El-Badry, K., Rix, H.-W., & Heintz, T. M. 2021, MNRAS, 506, 2269
El-Badry, K., Rix, H.-W., & Weisz, D. R. 2018, ApJL, 860, L17
Ferrario, L., de Martino, D., & Gänsicke, B. T. 2015, SSRv, 191, 111
Ferrario, L., Vennes, S., Wickramasinghe, D. T., Bailey, J. A., & Christian, D. J. 1997, MNRAS, 292, 205
Fields, C. E., Farmer, R., Petermann, I., Iliadis, C., & Timmes, F. X. 2016, ApJ, 823, 46
Finley, D. S., & Koester, D. 1997, ApJL, 489, L79
Fontaine, G., Brassard, P., & Bergeron, P. 2001, PASP, 113, 409
Foreman-Mackey, D., Hogg, D. W., Lang, D., & Goodman, J. 2013, PASP, 125, 306
Fouesneau, M., Rix, H.-W., von Hippel, T., Hogg, D. W., & Tian, H. 2019, ApJ, 870, 9
Gaia Collaboration, Prusti, T., de Bruijne, J. H. J., et al. 2016, A&A, 595, A1
Gaia Collaboration, Babusiaux, C., van Leeuwen, F., et al. 2018b, A&A, 616, A10
Gaia Collaboration, Brown, A. G. A., Vallenari, A., et al. 2021, A&A, 649, A1
Gentile Fusillo, N. P., Tremblay, P. E., Cukanovaite, E., et al. 2021, MNRAS, 508, 3877
Gaia Collaboration, Brown, A. G. A., & Vallenari, A. 2018a, A&A, 616, A1
Gentile Fusillo, N. P., Tremblay, P.-E., Gänsicke, B. T., et al. 2019, MNRAS, 482, 4570
Giammichele, N., Bergeron, P., & Dufour, P. 2012, ApJS, 199, 29
Gianninas, A., Bergeron, P., & Ruiz, M. T. 2011, ApJ, 743, 138
Goodman, J., & Weare, J. 2010, CAMCS, 5, 65
Guo, J., Zhao, J., Tziamtzis, A., et al. 2015, MNRAS, 454, 2787
Hut, P., & Bahcall, J. N. 1983, ApJ, 268, 319
Kalirai, J. S., Hansen, B. M. S., Kelson, D. D., et al. 2008, ApJ, 676, 594
Kepler, S. O., Kleinman, S. J., Nitta, A., et al. 2007, MNRAS, 375, 1315
Kepler, S. O., Pelisoli, I., Koester, D., et al. 2015, MNRAS, 446, 4078
Kepler, S. O., Pelisoli, I., Koester, D., et al. 2016, MNRAS, 455, 3413
Kepler, S. O., Pelisoli, I., Koester, D., et al. 2019, MNRAS, 486, 2169
Kilic, M., Bergeron, P., Dame, K., et al. 2019, MNRAS, 482, 965
Kilic, M., Bergeron, P., Kosakowski, A., et al. 2020, ApJ, 898, 84
Kiman, R., Faherty, J. K., Cruz, K. L., et al. 2021, AJ, 161, 277
Kleinman, S. J., Kepler, S. O., Koester, D., et al. 2013, ApJS, 204, 5
Koester, D. 2010, Mem. Soc. Astron. Italiana, 81, 921
Koester, D., Voss, B., Napiwotzki, R., et al. 2009, A&A, 505, 441
Kraus, A. L., & Hillenbrand, L. A. 2009, ApJ, 704, 531
Külebi, B., Jordan, S., Nelan, E., Bastian, U., & Altmann, M. 2010, A&A, 524, A36
Liebert, J., Bergeron, P., & Holberg, J. B. 2005, ApJS, 156, 47
Limoges, M. M., Lépine, S., & Bergeron, P. 2013, AJ, 145, 136
Marigo, P., Cummings, J. D., Curtis, J. L., et al. 2020, NatAs, 4, 1102
Marrese, P. M., Marinoni, S., Fabrizio, M., & Altavilla, G. 2021, Gaia EDR3 documentation Chapter 9: Cross-match with external catalogues, ESA
Martin, D. V., El-Badry, K., Hodžić, V. K., et al. 2021, MNRAS, 507, 4132
McCook, G. P., & Sion, E. M. 1999, ApJS, 121, 1
Moe, M., & Di Stefano, R. 2017, ApJS, 230, 15
Morgan, D. P., West, A. A., Garcés, A., et al. 2012, AJ, 144, 93
Moss, A., von Hippel, T., Robinson, E., et al. 2022, ApJ, 929, 26
Paxton, B., Bildsten, L., Dotter, A., et al. 2011, ApJS, 192, 3
Paxton, B., Cantiello, M., Arras, P., et al. 2013, ApJS, 208, 4
Paxton, B., Marchant, P., Schwab, J., et al. 2015, ApJS, 220, 15
Perpinyá-Vallés, M., Rebassa-Mansergas, A., Gänsicke, B. T., et al. 2019, MNRAS, 483, 901
Qiu, D., Tian, H.-J., Wang, X.-D., et al. 2021, ApJS, 253, 58
Rybizki, J., Green, G., Rix, H.-W., et al. 2022, MNRAS, 510, 2597
Salaris, M., Serenelli, A., Weiss, A., & Miller Bertolami, M. 2009, ApJ, 692, 1013
Schlafly, E. F., & Finkbeiner, D. P. 2011, ApJ, 737, 103
Sion, E. M., Oswalt, T. D., Liebert, J., & Hintzen, P. 1991, AJ, 101, 1476

Temmink, K. D., Toonen, S., Zapartas, E., Justham, S., & Gänsicke, B. T. 2020, A&A, 636, A31
Tian, H.-J., El-Badry, K., Rix, H.-W., & Gould, A. 2020, ApJS, 246, 4
Toonen, S., Boekholt, T. C. N., & Portegies Zwart, S. 2022, A&A, 661, A61
Torres, S., Rebassa-Mansergas, A., Camisassa, M. E., & Raddi, R. 2021, MNRAS, 502, 1753
Tremblay, P. E., Bergeron, P., & Gianninas, A. 2011, ApJ, 730, 128
Tremblay, P. E., Cummings, J., Kalirai, J. S., et al. 2016, MNRAS, 461, 2100
Tremblay, P. E., Kalirai, J. S., Soderblom, D. R., Cignoni, M., & Cummings, J. 2014, ApJ, 791, 92
Tremblay, P.-E., Fontaine, G., Gentile Fusillo, N. P., et al. 2019, Natur, 565, 202
Tremblay, P. E., Hollands, M. A., Gentile Fusillo, N. P., et al. 2020, MNRAS, 497, 130
Vennes, S., Schmidt, G. D., Ferrario, L., et al. 2003, ApJ, 593, 1040
White, R. J., & Ghez, A. M. 2001, ApJ, 556, 265
Winget, D. E., Hansen, C. J., Liebert, J., et al. 1987, ApJL, 315, L77
Zhang, Z., Liu, M. C., Hermes, J. J., et al. 2020, ApJ, 891, 171
Zhao, J. K., Oswalt, T. D., Willson, L. A., Wang, Q., & Zhao, G. 2012, ApJ, 746, 144